

# Dynamic control and quantification of active sites on ceria for CO activation and hydrogenation

W. Shao, P. Liu

To be published in "Nature Communications"

November 2024

Chemistry Department  
**Brookhaven National Laboratory**

**U.S. Department of Energy**  
USDOE Office of Science (SC), Basic Energy Sciences (BES)

Notice: This manuscript has been authored by employees of Brookhaven Science Associates, LLC under Contract No. DE-SC0012704 with the U.S. Department of Energy. The publisher by accepting the manuscript for publication acknowledges that the United States Government retains a non-exclusive, paid-up, irrevocable, world-wide license to publish or reproduce the published form of this manuscript, or allow others to do so, for United States Government purposes.

## **DISCLAIMER**

This report was prepared as an account of work sponsored by an agency of the United States Government. Neither the United States Government nor any agency thereof, nor any of their employees, nor any of their contractors, subcontractors, or their employees, makes any warranty, express or implied, or assumes any legal liability or responsibility for the accuracy, completeness, or any third party's use or the results of such use of any information, apparatus, product, or process disclosed, or represents that its use would not infringe privately owned rights. Reference herein to any specific commercial product, process, or service by trade name, trademark, manufacturer, or otherwise, does not necessarily constitute or imply its endorsement, recommendation, or favoring by the United States Government or any agency thereof or its contractors or subcontractors. The views and opinions of authors expressed herein do not necessarily state or reflect those of the United States Government or any agency thereof.

# Dynamic control and quantification of active sites on ceria for CO activation and hydrogenation

Weipeng Shao<sup>1,5</sup>, Yi Zhang<sup>2,5</sup>, Zhiwen Zhou<sup>2,5</sup>, Na Li<sup>2</sup>, Feng Jiao<sup>2</sup>, Yunjian Ling<sup>1,2</sup>, Yangsheng Li<sup>1,2</sup>, Zeyu Zhou<sup>1</sup>, Yunjun Cao<sup>2</sup>, Zhi Liu<sup>1</sup>, Xiulian Pan<sup>2</sup>, Qiang Fu<sup>2</sup>, Christof Wöll<sup>3</sup>, Ping Liu<sup>4</sup>, Xinhe Bao<sup>2</sup> & Fan Yang<sup>1,2</sup>

<sup>1</sup>School of Physical Science and Technology, Center for Transformative Science, ShanghaiTech University, Shanghai, China. <sup>2</sup>State Key Laboratory of Catalysis, Dalian Institute of Chemical Physics, Dalian, China. <sup>3</sup>Institute of Functional Interfaces, Karlsruhe Institute of Technology, Karlsruhe, Germany. <sup>4</sup>Chemistry Division, Brookhaven National Laboratory, Upton, New York, US. <sup>5</sup>These authors contributed equally: Weipeng Shao, Yi Zhang, Zhiwen Zhou. e-mail: [fyang@shanghaitech.edu.cn](mailto:fyang@shanghaitech.edu.cn)

Ceria (CeO<sub>2</sub>) is a widely used oxide catalyst, yet the nature of its active sites remains elusive. This study combines model and powder catalyst studies to elucidate the structure-activity relationships in ceria-catalyzed CO activation and hydrogenation. Well-defined ceria clusters are synthesized on planar CeO<sub>2</sub>(111) and exhibit dynamic and tunable ranges of Ce coordination numbers, which enhance their interaction with CO. Reduced ceria clusters (e.g., Ce<sub>3</sub>O<sub>3</sub>) bind CO strongly and facilitate its dissociation, while near-stoichiometric clusters (e.g., Ce<sub>3</sub>O<sub>7</sub>) adsorb CO weakly and promote oxidation via carbonate formation. Unlike planar ceria surfaces, supported ceria clusters exhibit dynamic properties and enhanced catalytic activity, that mimic those of powder ceria catalysts. Insight from model studies provide a method to quantify active sites on powder ceria and guide further optimization of ceria catalysts for syngas conversion. This work marks a leap toward model-guided catalyst design and highlights the importance of site-specific catalysis.

Metal oxide catalysts are widely used in the chemical industry and have been increasingly explored for catalytic hydrogenation reactions<sup>1-4</sup>, owing to their exceptional selectivity and stability. In syngas conversion, metal oxide nanocatalysts mixed with zeolites (OXZEO) exhibited exceptional catalytic performance<sup>5</sup>, where metal oxides were proposed to play a key role in CO activation while oxide surfaces were conventionally believed to interact weakly with CO<sup>6,7</sup>. So far, our understanding of the active sites of metal oxide catalysts has been limited, which led to a rudimentary approach in evaluating their intrinsic catalytic properties, typically involving the normalization of the reaction rate against the total surface area of metal oxides.

To unravel the structure-activity relationship of metal oxide catalysts, planar oxide surfaces were frequently employed as model systems. Although they allow for atomic-scale insights into the surface structure

of oxides<sup>5,7</sup> and can provide experimental information required for the validation of theoretical results<sup>8</sup>, bridging the materials gap between model systems and synthesized powder catalysts remains a formidable task<sup>9-12</sup>. While the catalytic properties of oxides are often attributed to surface defects, model studies have predominantly focused on surface oxygen vacancy<sup>1,13</sup>. Coordinatively unsaturated (cus) metal sites<sup>14-19</sup> have also attracted increasing interest in past years and have been extensively studied on planar oxide catalysts such as RuO<sub>2</sub>(110)<sup>16,17,19</sup>, IrO<sub>2</sub>(110)<sup>15,19</sup> and PdO(101)<sup>18,19</sup>. In contrast, practical metal oxide catalysts typically take the form of nanostructures (NSs)<sup>20</sup> and expose cus sites with diverse coordination numbers (CN)<sup>21</sup>. This complexity in their structure-activity relationship arises due to the interplay of several factors, including oxidation/electronic states, surface structural and compositional motifs, charge transfer, and unique size/shape characteristics<sup>1,21-25</sup>. To overcome

the intricate interdependencies in powder catalysts, it becomes imperative to study oxide NSs with tunable and well-defined surface structures, which enables the identification of active sites and the establishment of structure-activity relationships.

In this study, we synthesized well-defined oxide clusters on planar oxide surfaces, thereby facilitating an atomic-scale resolution of their intricacies. Using ceria catalysts as an example, our study integrated scanning tunneling microscopy (STM), synchrotron-radiation, and lab X-ray photoelectron spectroscopy (SRPES and XPS), density functional theory (DFT) calculations and model catalytic studies to examine their active-site structures and catalytic properties across a range of configurations by modifying the size, stoichiometry and CN of surface Ce sites ( $CN_{Ce}$ )<sup>26</sup>. We demonstrated that supported ceria clusters mimicked the structural and redox dynamics of powder ceria<sup>20,27-29</sup>, and controlled the reactivity of ceria in CO catalysis.

Ceria ( $CeO_x$ ) is among the most widely used oxide catalysts in heterogeneous catalysis<sup>30,31</sup>, and its superior catalytic performance is attributed to its ability to store and release oxygen<sup>23</sup>, the formation of cus-Ce sites and the facile transition between different oxidation states<sup>32</sup>. Nonetheless, its active-site structure, adsorption, and catalytic

properties have remained elusive. Through atomic-level studies of supported ceria clusters, planar ceria surfaces, and comparative analysis with powder ceria, we found that supported ceria clusters showed reaction properties similar to powder ceria and exhibited a dynamic and tunable range of  $CN_{Ce}$ , which correlates with CO activation and hydrogenation. The structure-reactivity relationship established through model studies can be extended to practical ceria catalysts and allow for the identification, quantification, and enhancement of active sites on ceria, leading to improved activity and selectivity for hydrocarbon production in syngas conversion.

## Results and discussion

**Synthesis of supported  $CeO_x$  model catalysts with different  $CN_{Ce}$**   
Well-ordered  $CeO_2(111)$  thin films and supported  $CeO_x$  clusters were prepared (see "Methods" for details). Figure 1a, b shows that the  $CeO_2(111)$  surface displays flat terraces and exhibits an ordered hexagonal lattice with an atomic spacing of 0.38 nm and a step height of 0.3 nm, corresponding to the thickness of an O-Ce-O trilayer (Supplementary Fig. 1). Although surface and subsurface oxygen vacancies have been suggested as primary defects on  $CeO_2(111)$ , their

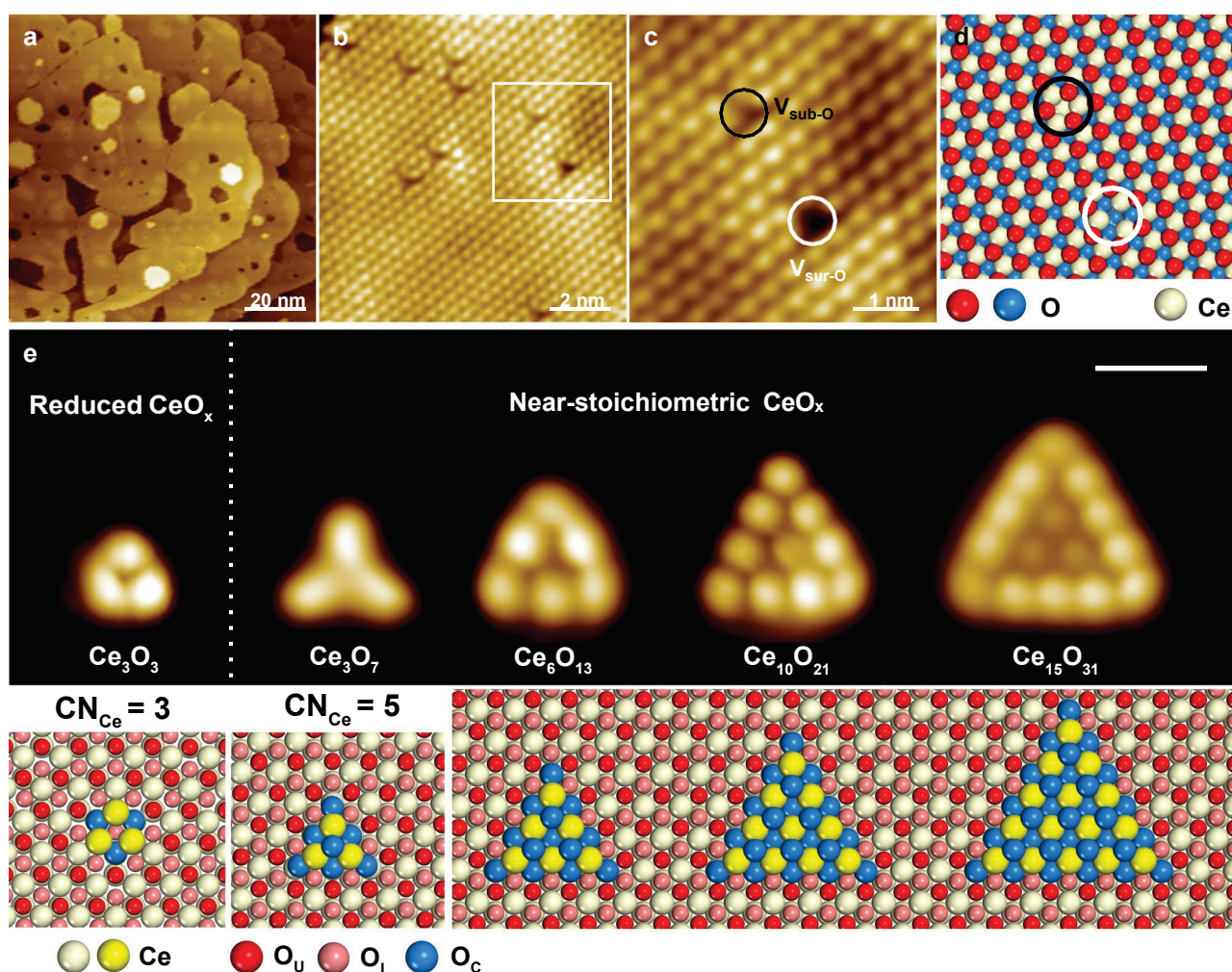


Fig. 1 Atomic structures of planar  $CeO_2(111)$  and well-defined ceria clusters. a Large-scale STM image of the  $CeO_2(111)$  film surface. b O-mode STM image of the  $CeO_2(111)$  surface. The squared area is magnified in (c), showing surface O vacancy ( $V_{sur-O}$ ) as a dark hole and sub-surface O vacancy ( $V_{sub-O}$ ) as a three-pointed depression star at the hollow site of O atoms. The  $CeO_2(111)$  surface is dominated by  $V_{sub-O}$ . d The corresponding structural model of O vacancies. Ce atoms, surface, and subsurface O atoms are displayed in white, red, and blue, respectively. e Atomic-resolution STM images (upper panel, scale bar: 1 nm) and the corresponding structural models of supported  $Ce_3O_3$ ,  $Ce_3O_7$ ,  $Ce_6O_{13}$ ,  $Ce_{10}O_{21}$ , and  $Ce_{15}O_{31}$  clusters (lower panel). DFT-optimized structural models of  $Ce_3O_3$  supported on  $Ce_2O_3(0001)$  and  $Ce_3O_7$  supported on  $CeO_2(111)$  are displayed with labels on their O-coordination numbers of Ce sites. Surface lattice parameters are close for  $Ce_2O_3(0001)$  and  $CeO_2(111)$ , which exhibited major differences in stacking along the vertical direction.  $O_U$ ,  $O_L$ , and  $O_C$  represent O atoms in the topmost O layer, the lower O layer, and supported  $CeO_x$  clusters, respectively.

identification has remained elusive<sup>25,33–35</sup>. Using element-specific STM (ES-STM) imaging<sup>36</sup>, we unambiguously identified surface and subsurface oxygen vacancies of CeO<sub>2</sub>(111). The O-mode STM images resolved surface O atoms as bright protrusions, while surface O vacancies were depicted as dark holes (Fig. 1b–d and Supplementary Fig. 2a). Conversely, subsurface O vacancies manifested as three-pointed depressions at the hollow sites of surface O lattice (Fig. 1b, c). In the Ce-mode STM image (Supplementary Fig. 2b), Ce atoms were discerned as bright protrusions, and the structure of oxygen vacancies was not readily apparent (Supplementary Fig. 2c, d).

Ceria clusters of varying shapes and sizes were deposited on CeO<sub>2</sub>(111) and exhibited high thermal stability at below 800 K<sup>37</sup>. CN<sub>Ce</sub> of supported ceria clusters could be adjusted by regulating the O<sub>2</sub> pressure during Ce deposition (Fig. 1e). Here, we emphasize two types of surfaces that are stable under catalytically realistic conditions, which we termed as the near-stoichiometric CeO<sub>x</sub> cluster (ns-CeO<sub>x</sub>) and reduced CeO<sub>x</sub> cluster (r-CeO<sub>x</sub>) surfaces, respectively. The former surface could be prepared by evaporating Ce in above  $3 \times 10^{-7}$  mbar O<sub>2</sub>, resulting in the formation of ns-CeO<sub>x</sub>, such as Ce<sub>3</sub>O<sub>7</sub>, Ce<sub>6</sub>O<sub>13</sub>, Ce<sub>10</sub>O<sub>21</sub>, and Ce<sub>15</sub>O<sub>31</sub> on CeO<sub>2</sub>(111) with CN<sub>Ce</sub> ≥ 5 (Fig. 1e and Supplementary Fig. 3a). In contrast, the latter surfaces were prepared by evaporating Ce in  $3 \times 10^{-8}$  mbar O<sub>2</sub>, leading to the growth of r-CeO<sub>x</sub>, such as Ce<sub>3</sub>O<sub>3</sub> or larger clusters on CeO<sub>2</sub>(111) with lower CN<sub>Ce</sub> (Fig. 1e and Supplementary Fig. 3c). As-prepared ceria clusters on both surfaces displayed a similar size distribution (Supplementary Fig. 3). Ce<sub>3</sub>O<sub>7</sub> and Ce<sub>3</sub>O<sub>3</sub> are the smallest clusters observed on each surface and could serve as the structural moiety for larger clusters, thus being representative of the oxidized and reduced states of ceria clusters on these two surfaces. Note that, the deposition of reduced CeO<sub>x</sub> clusters could result in local reduction of the ceria substrate underneath, as indicated by the substantial reduction of CeO<sub>2</sub>(111) in XPS (Supplementary Fig. 4). DFT calculations also showed that deposited Ce atom would reduce the neighboring substrate by pulling oxygen atoms towards Ce cations in reduced CeO<sub>x</sub> clusters (Supplementary Fig. 4). Subsequently, Ce atoms underneath reduced CeO<sub>x</sub> clusters tend to exhibit a structure similar to that of Ce<sub>2</sub>O<sub>3</sub>(0001)<sup>38,39</sup>. Highly reduced CeO<sub>x</sub> clusters could be prepared by evaporating Ce atoms in UHV, but are not stable in CO at elevated temperatures (Supplementary Figs. 5, 6). Their reaction properties (Supplementary Figs. 5–7) are discussed in Supplementary Note 1 and are not the focus of this work.

Figure 1e demonstrates the diverse array of triangular supported CeO<sub>x</sub> clusters, including Ce<sub>3</sub>O<sub>3</sub>, Ce<sub>3</sub>O<sub>7</sub>, Ce<sub>6</sub>O<sub>13</sub>, Ce<sub>10</sub>O<sub>21</sub>, and Ce<sub>15</sub>O<sub>31</sub>, which exhibited the same hexagonal lattice as CeO<sub>2</sub>(111) but displayed varied sizes and CN<sub>Ce</sub>. Their structures could be discerned from ES-STM images (Supplementary Fig. 8). From Ce<sub>3</sub>O<sub>3</sub> to Ce<sub>3</sub>O<sub>7</sub>, both the Ce valence state (Supplementary Fig. 9) and CN<sub>Ce</sub> increase, while the Ce lattice size remains mostly unchanged (Supplementary Fig. 3). As the cluster size expands from Ce<sub>6</sub>O<sub>13</sub>, Ce<sub>10</sub>O<sub>21</sub> to Ce<sub>15</sub>O<sub>31</sub>, the alterations in valence state and CN<sub>Ce</sub> are relatively insignificant, with clusters maintaining a near stoichiometry.

### CO activation and hydrogenation over supported CeO<sub>x</sub> model catalysts

Planar CeO<sub>2</sub>(111) and supported CeO<sub>x</sub> cluster surfaces were then exposed to CO respectively (Fig. 2) and showed drastically different reactivity towards CO. The CeO<sub>2</sub>(111) surface that corresponded to a high CN<sub>Ce</sub> of 7 showed no reactivity towards CO in UHV (Fig. 2a, b). Even after surface reduction to form CeO<sub>1.93</sub>, no chemisorption or reaction of CO was obvious on planar ceria surfaces at 300 K from UHV to ambient pressures (AP) in STM or AP-XPS (Fig. 2a–c and Supplementary Fig. 10). CO appeared as diffusive species at step edges in STM at 78 K (Supplementary Fig. 11), but no CO reaction was obvious at between 300–500 K (Fig. 2d), as previously reported<sup>40,41</sup>.

In contrast, supported ceria clusters demonstrated substantially higher reactivity towards CO. On the ns-CeO<sub>x</sub> surface, Fig. 2e–h

showed that adsorbates appeared at the corner or step sites of ceria clusters upon CO exposure at 300 K, and displayed similar apparent heights, often in the bidentate configuration. SRPES on the ns-CeO<sub>x</sub> surface suggested the formation of \*CO<sub>3</sub> species with a C 1s peak at 289.3 eV<sup>42</sup>, which partially decreased at 500 K, and completely vanished at 600 K due to carbonate decomposition and CO<sub>2</sub> desorption (Supplementary Fig. 12). On the r-CeO<sub>x</sub> surface, CO adsorption at 300 K produced a bright protrusion at the hollow site on Ce<sub>3</sub>O<sub>3</sub> (Fig. 2i, j), displaying an apparent height of ~0.6 Å higher than carbonate on Ce<sub>3</sub>O<sub>7</sub> (Fig. 2e and Supplementary Figs. 13, 14), and indicating a higher electronic density near the Fermi level (E<sub>F</sub>). SRPES on the r-CeO<sub>x</sub> surface detected an additional C 1s peak at 284.5 eV, suggesting the formation of \*C (Fig. 2k, l), which could be produced via the disproportionation reaction of CO, simultaneously generating CO<sub>2</sub> and \*C. CO<sub>2</sub> easily desorbed from the cluster surface, leaving \*C at the hollow site. Among the different-sized ceria clusters, no noticeable size effect was observed on the formation of \*CO<sub>3</sub> or \*C species.

Spin-polarized DFT calculations were performed to understand the reaction properties of above supported CeO<sub>x</sub> model catalysts. Based on STM measurements, Ce<sub>3</sub>O<sub>7</sub> supported on CeO<sub>2</sub>(111) (noted as Ce<sub>3</sub>O<sub>7</sub>) was constructed to represent the ns-CeO<sub>x</sub> surface. Ce<sub>3</sub>O<sub>4</sub> supported on Ce<sub>2</sub>O<sub>3</sub>(0001) (noted as Ce<sub>3</sub>O<sub>4</sub>), and Ce<sub>3</sub>O<sub>3</sub>/Ce<sub>2</sub>O<sub>3</sub>(0001) (noted as Ce<sub>3</sub>O<sub>3</sub>, Supplementary Fig. 15) were constructed to understand the r-CeO<sub>x</sub> surface. In our study, the fully oxidized Ce<sub>3</sub>O<sub>7</sub> cluster was stable only under the oxidizing conditions, and thus CeO<sub>2</sub>(111) was used as support. As the reduced Ce<sub>3</sub>O<sub>4</sub> and Ce<sub>3</sub>O<sub>3</sub> clusters were synthesized under reducing conditions, the Ce<sub>2</sub>O<sub>3</sub>(0001) substrate was taken into consideration due to the possible removal of surface oxygen upon Ce deposition and the preferential diffusion of oxygen vacancies from surface to bulk of ceria<sup>43</sup>. DFT calculations showed that reduced CeO<sub>x</sub> clusters supported on CeO<sub>2</sub>(111) are not stable, but prefer to reduce the surface by pulling the oxygen atoms outward and form an atomic configuration (Supplementary Fig. 4a) similar to that of Ce<sub>2</sub>O<sub>3</sub>(0001) as reported previously<sup>38</sup>. The CeO<sub>2</sub>(111) surface, Ce<sub>2</sub>O<sub>3</sub>(0001) surface and CeO<sub>2</sub>(111) step were included for comparison. CO was used to probe the adsorption property of the most active Ce site (Supplementary Fig. 16) on each model system and found to prefer cus-Ce sites on all systems. On planar ceria, both surface terraces and steps exhibited weak CO physisorption (Supplementary Fig. 16a, c) and no reaction with CO at 300 K (Fig. 2a–c). The binding energy of CO on Ce<sub>3</sub>O<sub>7</sub> is also rather weak (–0.21 eV) (Fig. 3a and Supplementary Fig. 16d), while the adsorption on Ce<sub>3</sub>O<sub>3</sub> is strengthened by 0.79 eV (Fig. 3a and Supplementary Fig. 16f). Consistent with experimental studies, DFT results showed that indeed the weak Ce–CO interaction on Ce<sub>3</sub>O<sub>7</sub> (Fig. 3b) results in the transition of adsorbed CO (\*CO) to carbonate (\*CO<sub>3</sub>) species at the Ce<sub>3</sub>O<sub>7</sub>–CeO<sub>2</sub>(111) interface, where a CO molecule interacts with oxygen from the corner site of Ce<sub>3</sub>O<sub>7</sub> cluster, as well as O and Ce atom from the ceria support (Fig. 3c). In contrast, with the strong Ce–CO binding on Ce<sub>3</sub>O<sub>3</sub>/Ce<sub>2</sub>O<sub>3</sub>(0001) (Fig. 3a, d), the cleavage of the C–O bond to form atomic carbon (\*C) is preferred (Fig. 3a, f), rather than the formation of \*CO<sub>3</sub> (Fig. 3e). In this case, the breakage of C–O bond undergoes the CO disproportionation reaction (2\*CO = CO<sub>2</sub> + \*C, Fig. 3a, g), which is energetically more favorable than the direct dissociation of \*CO (\*CO = \*C + \*O, Fig. 3a, f). The Ce<sub>3</sub>O<sub>3</sub>/Ce<sub>2</sub>O<sub>3</sub>(0001) system allows the direct exposure of active Ce with low CN<sub>Ce</sub> on the surface. As a result, the dissociated \*C can be well stabilized at the three-fold hollow site of Ce atoms (Fig. 3g), as observed in STM (Fig. 2i). Thus, the reduction in CN<sub>Ce</sub> from Ce<sub>3</sub>O<sub>7</sub> to Ce<sub>3</sub>O<sub>3</sub> along with the interfacial transformation could tune the favorable reaction pathway from the formation of \*CO<sub>3</sub> to \*C upon CO exposure, in agreement with experimental observations.

We then evaluated the influence of cluster size, the oxidation state of Ce and CN<sub>Ce</sub> in CO activation using CO adsorption energy as an indicator. A correlation could be observed for CO adsorption at the Ce site in the range of  $3 \leq \text{CN}_{\text{Ce}} \leq 7$  (Supplementary Fig. 17). The CO binding energy increases with the contraction of the Ce–C bond, and

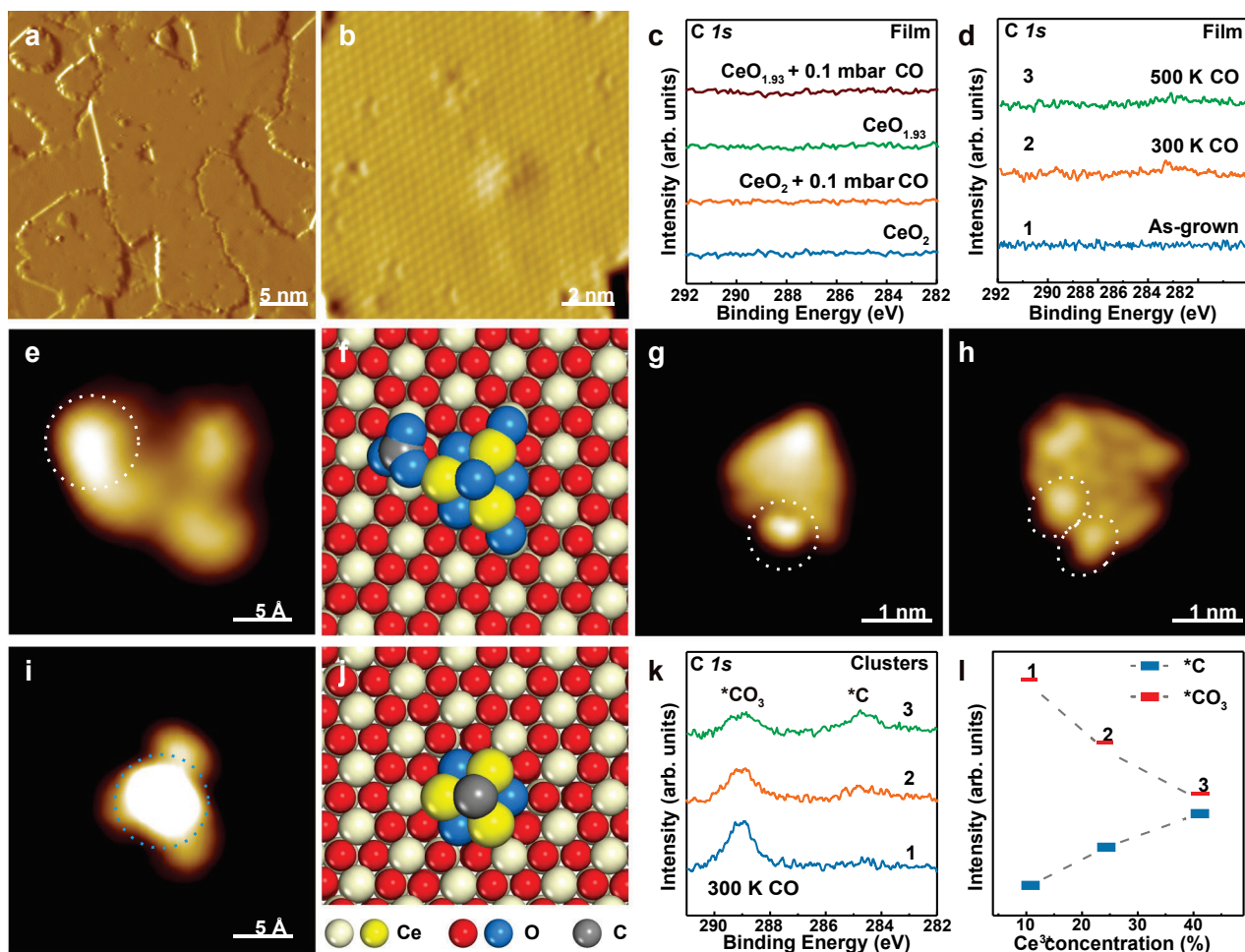


Fig. 2 CO interaction and reaction with the  $\text{CeO}_2(111)$  surface and ceria clusters supported on  $\text{CeO}_2(111)$ . a, b STM images of the  $\text{CeO}_2(111)$  surface after the exposure to 250 L CO at 300 K. c  $\text{C } 1s$  spectra of planar  $\text{CeO}_2(111)$  and reduced  $\text{CeO}_{2-x}(111)$  surfaces before and after the exposure to 0.1 mbar CO at 300 K. The stoichiometry of the reduced  $\text{CeO}_{2-x}(111)$  surface was determined as  $\text{CeO}_{1.93}$  by XPS  $\text{Ce } 3d$  spectra. d  $\text{C } 1s$  spectra of the  $\text{CeO}_2(111)$  film taken after sequential treatments: 1. the as-grown film; 2. the exposure of 250 L CO at 300 K; 3. the annealing to 500 K in  $5 \times 10^{-7}$  mbar CO and then cooling to 300 K in CO. e-h STM images of (e)  $\text{Ce}_3\text{O}_7$ , (g)  $\text{Ce}_{15}\text{O}_{31}$  and (h)  $\text{Ce}_{21}\text{O}_{43}$  clusters after the exposure to  $5 \times 10^{-7}$  mbar CO at 300 K. The corresponding structural model of  $\text{Ce}_3\text{O}_7$  after CO adsorption was shown in (f). Adsorbate could be observed at the corner site of  $\text{Ce}_3\text{O}_7$  and along the step/corner sites of  $\text{Ce}_{15}\text{O}_{31}$  and  $\text{Ce}_{21}\text{O}_{43}$ . i STM image of  $\text{Ce}_3\text{O}_3$  after the exposure to  $5 \times 10^{-7}$  mbar CO at 300 K. Adsorbate could be observed at the hollow site, and the corresponding structural model was shown in (j). k  $\text{C } 1s$  spectra of supported ceria clusters taken after exposing to 250 L CO at 300 K (1. the ns- $\text{CeO}_x$  surface; 2. supported ceria clusters prepared by evaporating Ce in  $1 \times 10^{-7}$  mbar  $\text{O}_2$  at 300 K onto  $\text{CeO}_2(111)$ ; 3. the r- $\text{CeO}_x$  surface). The intensities of carbonate and carbon peaks from (k) are plotted in (l), as a function of surface  $\text{Ce}^{3+}$  concentration, which was obtained from RPES taken simultaneously.

the decreasing of  $\text{CN}_{\text{Ce}}$  for the Ce site interacted (Supplementary Figs. 16, 17). Neither the oxidation state of Ce nor cluster size appeared as sensitive as  $\text{CN}_{\text{Ce}}$ . A decrease in the oxidation state of Ce from 4+ to 3+ could only increase CO binding by 0.07 eV when  $\text{CN}_{\text{Ce}}$  was kept at 6 for the  $\text{CeO}_2(111)$  step and  $\text{Ce}_2\text{O}_3(0001)$  surface. Meanwhile, for  $\text{Ce}_3\text{O}_x$  of similar cluster size, a significant increase in CO binding could be observed from  $\text{Ce}_3\text{O}_7$  (-0.21 eV) to  $\text{Ce}_3\text{O}_4$  (-0.82 eV) and  $\text{Ce}_3\text{O}_3$  (-1.0 eV). The mixed influence of  $\text{CN}_{\text{Ce}}$  and electronic effect cannot be disentangled for  $\text{Ce}_3\text{O}_x$ . However, DFT calculations corroborated that the enhanced reactivity of supported ceria clusters could be associated with a significant gain in the flexibility of  $\text{Ce}_3\text{O}_x$  (Supplementary Table 1 and Supplementary Note 2). Such flexibility enables variations in the local environment<sup>21</sup> around the interacted Ce site to accommodate and enhance the interaction with CO.

### Structural dynamics and catalytic properties of supported $\text{CeO}_x$ model catalysts during CO hydrogenation

The flexibility of supported  $\text{Ce}_3\text{O}_x$  clusters could be further demonstrated by their enhanced reactivity and structural dynamics in CO

hydrogenation (Fig. 4). When planar  $\text{CeO}_2(111)$  was exposed to the flowing  $\text{CO}/\text{H}_2$  (1:3) mixture gas, no appreciable reactivity was detected by on-line GC from 300 to 675 K (Supplementary Fig. 18). In contrast, when the ns- $\text{CeO}_x$  surface was heated in the same  $\text{CO}/\text{H}_2$  mixture gas, two main products,  $\text{CO}_2$  and  $\text{CH}_4$ , were observed throughout the reaction, with the former easily detected at above 500 K and the latter at above 575 K (Supplementary Fig. 18). Despite the similar oxidation state of planar ceria and the ns- $\text{CeO}_x$  surface (Fig. 4c), they exhibited orders-of-magnitude reactivity difference for CO hydrogenation. Quasi-in-situ XPS analysis suggested a significant reduction of Ce sites on the ns- $\text{CeO}_x$  surface from 5.6% to 42.3% (Fig. 4c, d), whereas planar ceria surfaces were only reduced from 3.2% to 8.9%.

On the ns- $\text{CeO}_x$  surface, two kinetic regimes were observed for the formation of  $\text{CO}_2$  (Fig. 4a), with the low-temperature regime requiring a high barrier (125 kJ/mol) and the high-temperature regime displaying a low barrier of 22.0 kJ/mol. The formation of  $\text{CH}_4$  in the high-temperature regime exhibited an apparent activation energy of 72.0 kJ/mol (Supplementary Fig. 18c). Interestingly, the r- $\text{CeO}_x$  surface showed an oxidation state similar to that of the ns- $\text{CeO}_x$  surface after

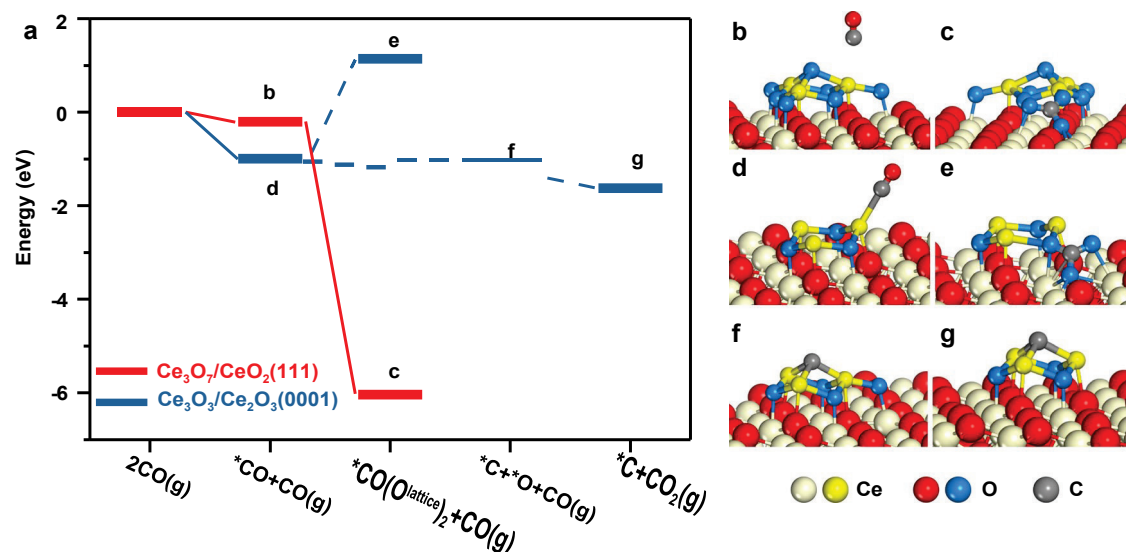


Fig. 3 DFT-calculated potential energy diagram for the reaction toward CO on  $\text{Ce}_3\text{O}_7/\text{CeO}_2(111)$  and  $\text{Ce}_2\text{O}_3/\text{Ce}_2\text{O}_3(0001)$ . a Reaction diagram together with the optimized geometries of reaction intermediates: (b)  $^*\text{CO}$  and (c)  $^*\text{CO}_3$  on  $\text{Ce}_3\text{O}_7/\text{CeO}_2(111)$ , (d)  $^*\text{CO}$ , (e)  $^*\text{CO}_3$ , (f)  $^*\text{C} + ^*\text{O}$  and (g)  $^*\text{C}$  on  $\text{Ce}_2\text{O}_3/\text{Ce}_2\text{O}_3(0001)$ .

CO hydrogenation (Fig. 4c, d). When the as-prepared r- $\text{CeO}_x$  surface was exposed to the same  $\text{CO}/\text{H}_2$  mixture gas, an onset production of  $\text{CO}_2$  yielded an apparent activation energy of 22.1 kJ/mol (Fig. 4b) and the production of  $\text{CH}_4$  yielded an apparent activation energy of 71.8 kJ/mol (Supplementary Fig. 19), similar to those of the ns- $\text{CeO}_x$  surface in the high-temperature regime. Post-reaction analysis of the r- $\text{CeO}_x$  surface also showed a similar Ce oxidation state and C 1s spectra as those of the ns- $\text{CeO}_x$  surface after CO hydrogenation (Fig. 4d, e). XPS C 1s spectra suggested that both surfaces resulted in a facile CO disproportionation reaction to produce  $\text{CO}_2$  and  $^*\text{C}$  (Fig. 4e), as also demonstrated by the r- $\text{CeO}_x$  surface in UHV (Fig. 2i, k). In the  $\text{CO}/\text{H}_2$  mixture gas, the  $^*\text{C}$  species were subsequently hydrogenated to produce  $\text{CH}_4$ . Combining reaction kinetics and XPS analysis suggested that a high-pressure CO hydrogenation reaction could reduce the ns- $\text{CeO}_x$  surface into the r- $\text{CeO}_x$  surface, which involved an induction period and resulted in the low-temperature kinetic regime of ns- $\text{CeO}_x$ , where the decomposition of carbonate to  $\text{CO}_2$  requires a large barrier<sup>44</sup>. Only upon the reduction to the r- $\text{CeO}_x$  surface did the disproportionation reaction of CO become feasible, producing  $\text{CO}_2$ .

While the  $^*\text{C}$  and  $^*\text{CO}_3$  species were observed on the ns- $\text{CeO}_x$  and r- $\text{CeO}_x$  surfaces after CO hydrogenation, planar ceria surfaces remained clean throughout the reaction range up to 675 K (Fig. 4e). The limited reactivity of planar ceria surfaces could originate from the lack of surface cus-Ce sites ( $\text{CN}_{\text{Ce}} \leq 5$ ). ES-STM images have suggested that oxygen vacancies are concealed in  $\text{CeO}_2(111)$  and preferentially located at subsurfaces (Fig. 1b), while the surface consists of < 1% O vacancies. Even after the reduction by CO at 800 K and above, we did not observe an obvious change in the density of surface O vacancies (Supplementary Fig. 20). The reduction in Ce oxidation state, in this case, is not indicative of active sites on planar ceria.

In contrast to planar  $\text{CeO}_2(111)$ , the drastic reduction of ns- $\text{CeO}_x$  to r- $\text{CeO}_x$  and its superior activity imply a significant role of cus-Ce sites on ceria clusters in CO hydrogenation under catalytically realistic conditions. By varying  $\text{CN}_{\text{Ce}}$ , not only the binding properties of Ce sites can be tuned, thus enhancing their catalytic activity, but also new reaction routes can be opened, thus changing selectivity. Our study shows that planar  $\text{CeO}_2$  surfaces tend to conceal oxygen vacancies inside the bulk, and eventually transform to  $\text{Ce}_2\text{O}_3$  at the surface layer, making it challenging to form cus-Ce sites active towards CO. In contrast, such cus-Ce sites are predominantly exposed at the edges of supported ceria clusters, which enable enhanced activity and tuned selectivity.

### Quantification of active sites and improving powder ceria catalysts for CO hydrogenation

The dynamic transformation between ns- $\text{CeO}_x$  and r- $\text{CeO}_x$  surfaces, as well as their adsorption and catalytic properties, are indeed analogous to those of powder ceria catalysts during CO activation and hydrogenation (Fig. 4c, d). Powder ceria catalysts, typically in the shape of nanoparticle ( $\text{CeO}_2\text{-N}$ ) or rod ( $\text{CeO}_2\text{-R}$ ), were synthesized and all exhibited the same fluorite structure (Supplementary Fig. 21). A series of  $\text{CeO}_2\text{-N}$  catalysts were prepared by varying their calcination temperatures at 673 K, 1073 K, and 1473 K, which were named  $\text{CeO}_2\text{-673}$ ,  $\text{CeO}_2\text{-1073}$ , and  $\text{CeO}_2\text{-1473}$ , respectively. From X-ray diffraction (XRD), these ceria catalysts exhibited different average crystallite sizes at 7.9, 75, and 117 nm (Supplementary Table 2 and Fig. 21). Meanwhile, a  $\text{CeO}_2\text{-R}$  catalyst was prepared and calcined at 573 K, termed as  $\text{CeO}_2\text{-573}$ , with an average crystallite size of 9.9 nm (Supplementary Table 2). The morphology, crystal facets, and particle size of these synthesized powder catalysts (Supplementary Fig. 22) were confirmed by high-resolution transmission electron microscopy (TEM), corroborating with XRD analysis.

Upon CO exposure at room temperature, our FT-IR measurements (Supplementary Fig. 23a) showed the spontaneous formation of  $^*\text{CO}_3$  species, in agreement with FT-IR studies<sup>10,45</sup>. Upon the reduction by CO, the formation of surface  $^*\text{C}$  species, in addition to  $^*\text{CO}_3$ , could be further observed in XPS on ceria catalysts (Supplementary Fig. 23b). Meanwhile, an online mass spectrometer (MS) detected  $\text{CO}_2$  production at above 473 K, and the subsequent annealing in  $\text{H}_2$  resulted in the observation of hydrocarbons such as ionized  $\text{CH}_4$  and  $\text{C}_2\text{H}_x$  species, indicating CO disproportionation reaction on ceria (Supplementary Fig. 24).

When powder ceria was employed for CO hydrogenation, an induction period for the production of  $\text{CO}_2$  was observed (Supplementary Fig. 25a), similar to that on the ns- $\text{CeO}_x$  surface. However, when powder ceria was pre-reduced in  $\text{H}_2$ , the induction period was eliminated, and a steady-state  $\text{CO}_2$  production could be observed with a reaction rate similar to that without  $\text{H}_2$  treatment (Supplementary Fig. 25b, c). Thus, the observed CO hydrogenation activities on powder ceria depend strongly on the low  $\text{CN}_{\text{Ce}}$  sites generated under reducing conditions, as demonstrated in model studies. Post-reaction XPS analysis showed a significant reduction of powder ceria during CO hydrogenation, which led to the concentration increase of  $\text{Ce}^{3+}$  sites from ~ 4% to 46.2% (Fig. 4c, d), similar to the behavior of the ns- $\text{CeO}_x$  surface. The similar adsorption and reaction properties between powder ceria and the ns- $\text{CeO}_x$  surface suggested that  $\text{Ce}_3\text{O}_7$  could

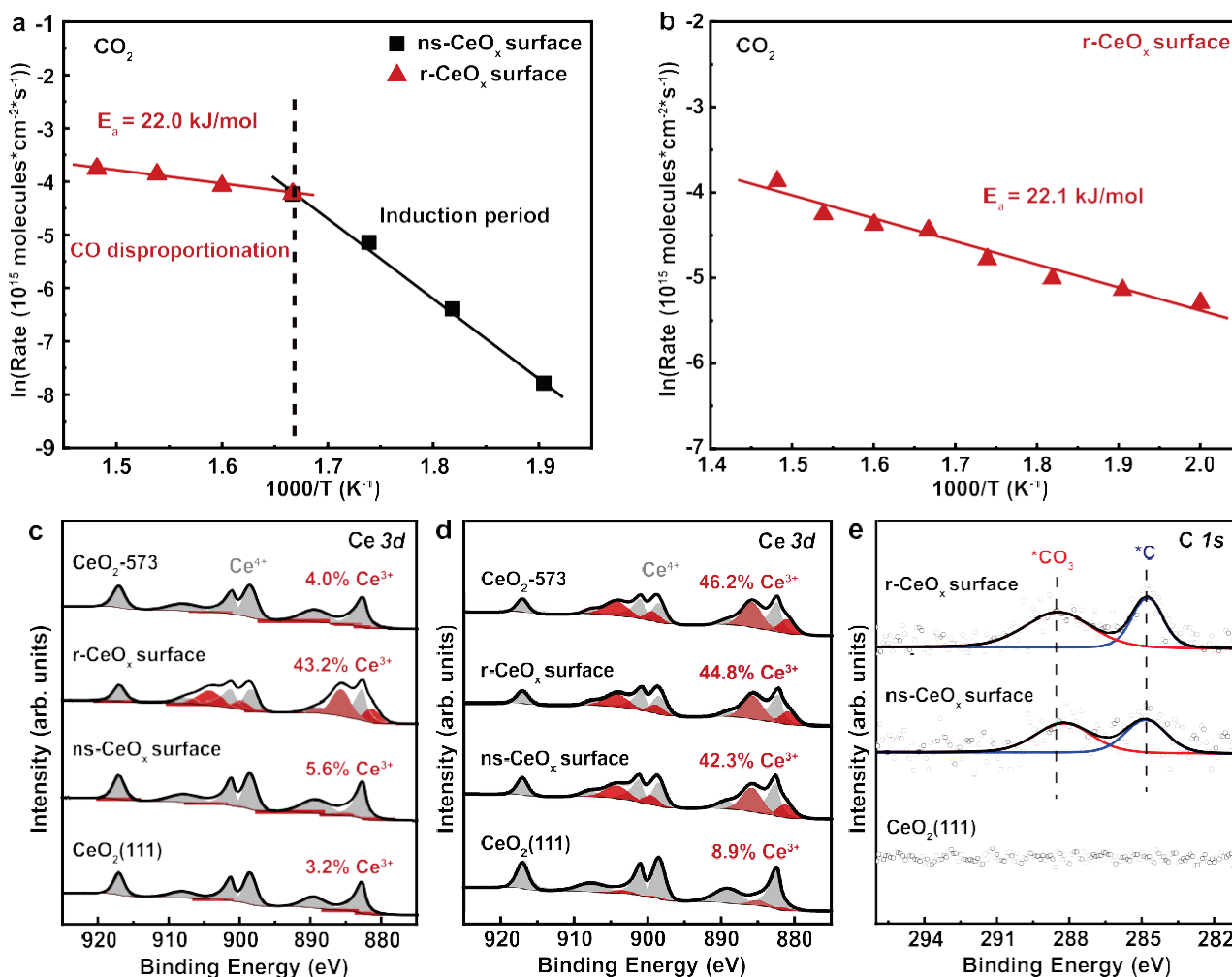


Fig. 4 Comparison of reaction kinetics, surface valence states, and chemical properties of model and powder ceria catalysts. The Arrhenius plots of reaction rates for CO hydrogenation to CO<sub>2</sub> were displayed for (a) the ns-CeO<sub>x</sub> surface and (b) the r-CeO<sub>x</sub> surface. XPS Ce 3*d* spectra of planar CeO<sub>2</sub>(111), the ns-CeO<sub>x</sub> surface, the r-CeO<sub>x</sub> surface, and CeO<sub>2</sub>-573 catalysts were compared (c) before and (d) after the CO hydrogenation reaction. e XPS C 1*s* spectra of the ns-CeO<sub>x</sub> surface, the r-CeO<sub>x</sub> surface, and planar CeO<sub>2</sub>(111) after the CO hydrogenation reaction.

serve as a structural analog for active sites on powder ceria, which underwent the same reductive transformation as the transformation from ns-CeO<sub>x</sub> to r-CeO<sub>x</sub> surfaces under CO hydrogenation reaction condition. As such, model understanding acquired from ns-CeO<sub>x</sub>/r-CeO<sub>x</sub> surfaces could guide the quantification and optimization of active sites on practical ceria catalysts.

Our model studies have shown that supported ceria clusters were not stable at above 800 K. Thus, varying the calcination temperature of powder ceria might be able to control the surface density of active sites. The series of ceria catalysts calcined at varying temperatures were tested for CO hydrogenation. Figure 5 showed that the space-time yields<sup>46</sup> of hydrocarbon increase from 38 μmol·g<sup>-1</sup>·h<sup>-1</sup> for CeO<sub>2</sub>-1473 to 1336 μmol·g<sup>-1</sup>·h<sup>-1</sup> for CeO<sub>2</sub>-573 with decreasing calcination temperature. The increase in space-time yield remains distinct from CeO<sub>2</sub>-673 (966.8 μmol·g<sup>-1</sup>·h<sup>-1</sup>) to CeO<sub>2</sub>-573 despite their similar crystallite size from XRD (Supplementary Table 2). XPS Ce 3*d* spectra (Supplementary Fig. 26) showed that four ceria catalysts all exhibited similar concentrations of Ce<sup>3+</sup> sites (~ 4%) upon calcination. Thus, XPS measurement of Ce oxidation state or XRD measurement of ceria crystallite size is not sensitive to active sites on powder ceria catalysts<sup>21</sup>.

However, the above model studies have shown that active sites on ceria are susceptible to carbonate formation upon CO exposure. That means, IR measurements of surface carbonates could be employed to

quantify active sites on powder ceria and showed drastic intensity differences among the four ceria catalysts (Supplementary Fig. 27). Indeed, reaction rates of these ceria catalysts were found to scale linearly with the normalized carbonate intensity from IR (Fig. 5), regardless their different size, shape or oxidation state. Our results confirm that the calcination treatment could be used to control the density of active Ce sites on powder ceria for CO activation and CO hydrogenation, which could be probed by IR.

To promote the catalytic performance of CO hydrogenation, we further mixed CeO<sub>2</sub>-T (*T* = 573, 673, 1073, 1473) catalysts with SAPO-34 zeolites. Previous study<sup>5</sup> suggested that adding zeolites could greatly facilitate the conversion of CH<sub>x</sub> species produced on partially reduced oxides into hydrocarbons, thereby pushing the reaction equilibrium of CO conversion forward. Consistently, the addition of SAPO-34 significantly increased CO conversion and selectivity towards light olefins (Fig. 5 and Supplementary Fig. 28). In combination with SAPO-34, CeO<sub>2</sub>-573 achieves a much higher CO conversion of 19.7% than other CeO<sub>2</sub>-T catalysts. The activity of mixed catalysts (CO conversion) still exhibited a linear relationship with the active-site density measured from normalized carbonate intensity, rather than with the particle size or oxidation state of powder ceria.

In summary, the combined model and powder catalytic studies demonstrated the pivotal role of dynamically transforming ceria

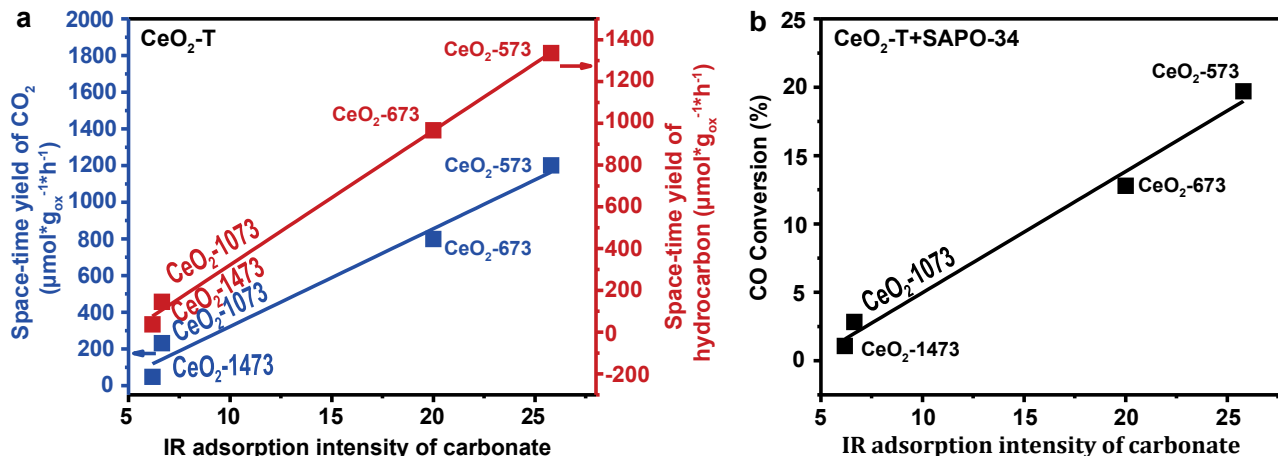


Fig. 5| The relationship between syngas conversion performance and the surface density of active sites on (a) CeO<sub>2</sub>-T and (b) CeO<sub>2</sub>-T/SAPO-34 ( $T = 573, 673, 1073, 1473$  K). The surface densities of active sites were measured by IR adsorption intensity of surface carbonate normalized by IR adsorption intensity of CO at 130 K. Reaction conditions for syngas conversion: CO/H<sub>2</sub> = 1/2.5, 673 K, 4.0 MPa and gas hourly space velocity (GHSV) = 2400 mL·h<sup>-1</sup>·g<sup>-1</sup> CeO<sub>x</sub>/SAPO-34 = 2/1 (mass ratio) in composite. The absorbance of carbonate was derived from FT-IR spectra after exposing CeO<sub>2</sub>-T catalysts to CO at 300 K.

clusters in CO activation and hydrogenation. By synthesizing well-defined ceria clusters on planar CeO<sub>2</sub>(111) with tailored CN<sub>Ce</sub>, we examined their structures, adsorption, and catalytic properties at the atomic level with an integrated approach using STM, SRPES, XPS, DFT calculations, and model catalytic studies. In contrast to planar ceria surfaces, supported ceria clusters exhibited dynamic and tunable ranges of CN<sub>Ce</sub>, which correlates with their much-enhanced activity towards CO activation and hydrogenation. We found that r-CeO<sub>x</sub> (e.g., Ce<sub>3</sub>O<sub>3</sub>) binds CO strongly and facilitates CO dissociation to atomic carbon and subsequent hydrogenation, whereas ns-CeO<sub>x</sub> (e.g., Ce<sub>3</sub>O<sub>7</sub>) binds CO weakly and preferentially promotes CO oxidation via carbonate formation.

Importantly, the dynamic reduction of the ns-CeO<sub>x</sub> surface to the r-CeO<sub>x</sub> surface during CO hydrogenation demonstrates the flexibility of supported ceria clusters similar to powder ceria catalysts. Atomic-level understanding from model studies could transfer effectively to practical ceria catalysts. We showed that their catalytic activity for CO hydrogenation can be distinguished by neither the particle size from XRD nor the Ce oxidation state from XPS. Rather, active sites on ceria could be titrated via carbonation formation as suggested by model studies and measured from IR. The carbonate intensity showed a linear relationship with CO conversion over ceria or its composite catalysts. By modulating the pre-treatment and activation procedures to maximize active site density, we improved the performance of powder ceria catalysts for CO hydrogenation. The understanding of active sites on ceria and the methodologies developed in this study could have general implications for studying complex oxide catalysts.

## Methods

### Model catalyst preparation and characterization

STM experiments were carried out in a combined ultrahigh vacuum (UHV) system, equipped with low-temperature scanning tunneling microscopy (LT-STM, Createc), XPS, UPS, and the cleaning facilities. The base pressures of STM and the preparation chamber are  $4 \times 10^{-11}$  and  $5 \times 10^{-11}$  mbar, respectively. All STM images were taken at 78 K and processed with SPIP software from Image Metrology (Denmark). Synchrotron-radiation photoelectron spectroscopy (SRPES) measurements were performed at the BL11U beamline in the National Synchrotron Radiation Laboratory (NSRL), China. The end station of the BL11U beamline is a combined UHV system including the analysis chamber, the preparation chamber, molecular beam epitaxy (MBE) chamber, and a radial distribution chamber. The base pressures are

$7 \times 10^{-11}$ ,  $1 \times 10^{-10}$ ,  $5 \times 10^{-10}$ , and  $2 \times 10^{-11}$  mbar, respectively. The analysis chamber is equipped with a VG Scienta R4000 analyzer, a monochromatic Al K<sub>α</sub> X-ray source, a UV light source, low energy electron diffraction (LEED), and a flood electron gun.

Well-ordered CeO<sub>2</sub>(111) thin film was prepared on Pt(111) by evaporating Ce in  $1 \times 10^{-7}$  mbar O<sub>2</sub>. Pt(111) single crystal (MaTeck) was cleaned by cycles of Ar ion sputtering and annealing up to 1000 K. Surface cleanliness was verified by STM and XPS. To ensure the full coverage of the metal substrate and the crystalline quality of ceria thin film, a kinetically limited growth process was adopted to grow CeO<sub>2</sub>(111)<sup>22</sup>. STM studies on as-prepared CeO<sub>2</sub>(111) thin films with varying thickness observed the same surface structure and found no obvious change in the concentration of surface defects on CeO<sub>2</sub>(111) (Supplementary Fig. 29). For reactivity measurements, CeO<sub>2</sub>(111) single crystals (Surfnet, Germany) and CeO<sub>2</sub>(111)/YSZ(111) were used to remove the influence of metal substrates. Supported ceria clusters of different CN<sub>Ce</sub> were prepared on CeO<sub>2</sub>(111) by controlling the O<sub>2</sub> pressure for Ce deposition. Details of model catalyst preparation and characterization are given in Supplementary Methods.

### Powder catalyst preparation and characterization

CeO<sub>2</sub> powder catalysts were prepared by precipitating cerium nitrate with urea in aqueous solution<sup>47</sup>. 21.71 g Ce(NO<sub>3</sub>)<sub>3</sub>·6H<sub>2</sub>O (Aladdin, AR), 12.61 g C<sub>2</sub>H<sub>2</sub>O<sub>4</sub> (tansoole, AR), and 9.01 g CO(NH<sub>2</sub>)<sub>2</sub> (General-reagent, AR) were added into 50 mL distilled water with continuous stirring for 1 h. Then the mixed solution was transferred into a 100 mL autoclave and heated to 413 K for 12 h. After filtering and washing several times with distilled water, the resulting precipitates were dried overnight at 353 K and then calcined at 673 K for 3 h. The obtained catalyst was named CeO<sub>2</sub>-673. The catalysts CeO<sub>2</sub>-1073 and CeO<sub>2</sub>-1473 were prepared by further calcining CeO<sub>2</sub>-673 at 1073 K and 1473 K in air for 3 h separately.

Powder ceria with an average crystal size of 9.9 nm was synthesized by a hydrothermal method. First, 24.0 g NaOH (General-reagent, AR) was added to Ce(NO<sub>3</sub>)<sub>3</sub>·6H<sub>2</sub>O (Aladdin, AR) (1.736 g to 80 mL of Millipore water) with continuous stirring for 0.5 h. Then the mixed solution was transferred into a 100 mL autoclave and heated to 383 K for 24 h. After filtering and washing several times with distilled water, the resulting precipitates were dried overnight at 333 K and then calcined at 573 K for 3 h. The obtained catalyst was named CeO<sub>2</sub>-573.

X-ray diffraction (XRD), N<sub>2</sub> adsorption-desorption, X-ray photoelectron spectroscopy (XPS), Fourier Transform infrared spectroscopy

(FT-IR), Transmission electron microscopy (TEM) and temperature-programmed surface reaction (TPSR) were used to measure the size, surface area, valence state, CO interaction with powder ceria, morphology and reactivity of ceria catalysts. The catalytic activity was measured in a fixed-bed reactor. Details of powder catalyst characterization are given in Supplementary Methods.

### Catalytic activity measurements

Reactivity measurements on model catalytic systems were performed on planar CeO<sub>2</sub>(111) surfaces and supported ceria clusters during CO hydrogenation in a high-pressure quartz fixed bed reactor cell (HPRC). HPRC was directly connected to a UHV system, consisting of an XPS (Thermo-Fisher ESCALAB 250Xi) chamber and an MBE chamber. XPS was used to monitor catalyst samples before and after the reaction. Both CeO<sub>2</sub>(111) single crystals and CeO<sub>2</sub>(111)/YSZ(111) were tested and showed little differences from the substrates. Details of reactivity measurements and powder catalytic tests are given in Supplementary Methods.

### Computational methods

DFT calculations were performed with the Perdew-Burke-Ernzerhof (PBE) exchange-correlation functional<sup>48,49</sup> in a projector augmented-wave (PAW) implementation<sup>50</sup> using the Vienna ab initio simulation packages (VASP). A cutoff energy of 400 eV for the plane-wave basis set was employed for slab calculation and 700 eV for bulk calculation to obtain optimized lattice parameters. To obtain faster convergence, thermal smearing of one-electron states ( $k_B T = 0.05$  eV) was allowed using the Gaussian smearing method to define the partial occupancies. The DFT + U formalism was used to describe the localized (strongly correlated) *d*f electrons in cerium, as implemented by Dudarev<sup>51</sup>. To describe Ce,  $U_{ce} - J_{ce} = 3.0$  eV was used, which was shown previously to describe the surface chemistry of ceria appropriately with the DFT(GGA) + U method<sup>52–54</sup>. All structures were well converged until the forces decreased to less than 0.02 eV/Å. More details on the model construction and computation are described in Supplementary Methods.

### Data availability

The data that support the findings of this study are available from the corresponding authors upon request. Source data are provided in this paper.

### References

1. Vohs, J. M. Site requirements for the adsorption and reaction of oxygenates on metal oxide surfaces. *Chem. Rev.* 113, 4136–4163 (2013).
2. Stacchiola, D. J., Senanayake, S. D., Liu, P. & Rodriguez, J. A. Fundamental studies of well-defined surfaces of mixed-metal oxides: Special properties of MO<sub>x</sub>/TiO<sub>2</sub>(110) {M = V, Ru, Ce, or W}. *Chem. Rev.* 113, 4373–4390 (2013).
3. Dai, Y. et al. Recent progress in heterogeneous metal and metal oxide catalysts for direct dehydrogenation of ethane and propane. *Chem. Soc. Rev.* 50, 5590–5630 (2021).
4. Vilé, G., Bridier, B., Wichert, J. & Pérez-Ramírez, J. Ceria in hydrogenation catalysis: High selectivity in the Conversion of Alkynes to Olefins. *Angew. Chem. Int. Ed.* 51, 8620–8623 (2012).
5. Jiao, F. et al. Selective conversion of syngas to light olefins. *Science* 351, 1065–1068 (2016).
6. Diebold, U., Li, S. C. & Schmid, M. Oxide surface science. *Annu. Rev. Phys. Chem.* 61, 129–148 (2010).
7. Henrich, V. E. & Cox, P. A. *The Surface Science of Metal Oxides*. (Cambridge University Press, England, 1996).
8. Lustemberg, P. G. et al. Vibrational frequencies of Cerium-Oxide-Bound CO: A challenge for conventional DFT methods. *Phys. Rev. Lett.* 125, 256101 (2020).
9. Wang, Y. M. & Wöll, C. IR spectroscopic investigations of chemical and photochemical reactions on metal oxides: bridging the materials gap. *Chem. Soc. Rev.* 46, 1875–1932 (2017).
10. Caulfield, L., Sauter, E., Idriss, H., Wang, Y. & Wöll, C. Bridging the pressure and materials gap in heterogeneous catalysis: A combined UHV, in situ, and operando study using infrared spectroscopy. *J. Phys. Chem. C* 127, 14023–14029 (2023).
11. Freund, H. J. et al. Bridging the pressure and materials gaps between catalysis and surface science: clean and modified oxide surfaces. *Top. Catal.* 15, 201–209 (2001).
12. Assmann, J. et al. Heterogeneous oxidation catalysis on ruthenium: bridging the pressure and materials gaps and beyond. *J. Phys. Condens. Matter* 20, 184017 (2008).
13. Setvin, M., Wagner, M., Schmid, M., Parkinson, G. S. & Diebold, U. Surface point defects on bulk oxides: atomically-resolved scanning probe microscopy. *Chem. Soc. Rev.* 46, 1772–1784 (2017).
14. Fu, Q. et al. Interface-confined ferrous centers for catalytic oxidation. *Science* 328, 1141–1144 (2010).
15. Liang, Z., Li, T., Kim, M., Asthagiri, A. & Weaver, J. F. Low-temperature activation of methane on the IrO<sub>2</sub>(110) surface. *Science* 356, 299–303 (2017).
16. Over, H. Surface chemistry of ruthenium dioxide in heterogeneous catalysis and electrocatalysis: from fundamental to applied research. *Chem. Rev.* 112, 3356–3426 (2012).
17. Over, H. et al. Atomic-scale structure and catalytic reactivity of the RuO<sub>2</sub>(110) surface. *Science* 287, 1474–1476 (2000).
18. Weaver, J. F., Hakanoglu, C., Antony, A. & Asthagiri, A. High selectivity for primary C-H bond cleavage of propane  $\sigma$ -complexes on the PdO(101) surface. *J. Am. Chem. Soc.* 133, 16196–16200 (2011).
19. Weaver, J. F., Hakanoglu, C., Antony, A. & Asthagiri, A. Alkane activation on crystalline metal oxide surfaces. *Chem. Soc. Rev.* 43, 7536–7547 (2014).
20. Huang, W. X. Oxide nanocrystal model catalysts. *Acc. Chem. Res.* 49, 520–527 (2016).
21. Shi, J. J. et al. High-performance water gas shift induced by asymmetric oxygen vacancies: Gold clusters supported by ceria-praseodymia mixed oxides. *Appl. Catal. B* 301, 120789 (2022).
22. Jerratsch, J.-F. et al. Electron localization in defective ceria films: A study with scanning-tunneling microscopy and density-functional theory. *Phys. Rev. Lett.* 106, 246801 (2011).
23. Paier, J., Penschke, C. & Sauer, J. Oxygen defects and surface chemistry of ceria: Quantum chemical studies compared to experiment. *Chem. Rev.* 113, 3949–3985 (2013).
24. Suntivich, J., May, K. J., Gasteiger, H. A., Goodenough, J. B. & Shao-Horn, Y. A perovskite oxide optimized for oxygen evolution catalysis from molecular orbital principles. *Science* 334, 1383–1385 (2011).
25. Esch, F. et al. Electron localization determines defect formation on ceria substrates. *Science* 309, 752–755 (2005).
26. Mullins, D. R. The surface chemistry of cerium oxide. *Surf. Sci. Rep.* 70, 42–85 (2015).
27. Yang, C. W. et al. Surface faceting and reconstruction of ceria nanoparticles. *Angew. Chem. Int. Ed.* 56, 375–379 (2017).
28. Muravev, V. et al. Size of cerium dioxide support nanocrystals dictates reactivity of highly dispersed palladium catalysts. *Science* 380, 1174–1179 (2023).
29. Cargnello, M. et al. Control of metal nanocrystal size reveals metal-support interface role for ceria catalysts. *Science* 341, 771–773 (2013).
30. Rodriguez, J. A., Grinter, D. C., Liu, Z., Palomino, R. M. & Senanayake, S. D. Ceria-based model catalysts: fundamental studies on the importance of the metal-ceria interface in CO oxidation, the water-gas shift, CO<sub>2</sub> hydrogenation, and methane and alcohol reforming. *Chem. Soc. Rev.* 46, 1824–1841 (2017).
31. Trovarelli, A. *Catalysis by Ceria and Related Materials*. (Imperial College Press, London, England, 2002).

32. Yang, F. et al. CO Oxidation on inverse CeO<sub>x</sub>/Cu(111) catalysts: High catalytic activity and ceria-promoted dissociation of O<sub>2</sub>. *J. Am. Chem. Soc.* 133, 3444–3451 (2011).
33. Yang, C. W. et al. O<sub>2</sub> activation on ceria catalysts—the importance of substrate crystallographic orientation. *Angew. Chem. Int. Ed. Engl.* 56, 16399–16404 (2017).
34. Kullgren, J. et al. Oxygen vacancies versus fluorine at CeO<sub>2</sub>(111): A case of mistaken identity? *Phys. Rev. Lett.* 112, 156102 (2014).
35. Wu, X.-P. & Gong, X.-Q. Clustering of oxygen vacancies at CeO<sub>2</sub>(111): Critical role of hydroxyls. *Phys. Rev. Lett.* 116, 086102 (2016).
36. Zhu, B. et al. Vacancy ordering in ultrathin copper oxide films on Cu(111). *J. Am. Chem. Soc.* 146, 15887–15896 (2024).
37. Zhang, Y., Feng, W., Yang, F. & Bao, X. Interface-controlled synthesis of CeO<sub>2</sub>(111) and CeO<sub>2</sub>(100) and their structural transition on Pt(111). *Chin. J. Catal.* 40, 204–213 (2019).
38. Fronzi, M., Soon, A., Delley, B., Traversa, E. & Stampfl, C. Stability and morphology of cerium oxide surfaces in an oxidizing environment: A first-principles investigation. *J. Chem. Phys.* 131, 104701 (2009).
39. Xiao, W. D., Guo, Q. L. & Wang, E. G. Transformation of CeO<sub>2</sub>(111) to Ce<sub>2</sub>O<sub>3</sub>(0001) films. *Chem. Phys. Lett.* 368, 527–531 (2003).
40. Yang, C. W. et al. Chemical activity of oxygen vacancies on ceria: a combined experimental and theoretical study on CeO<sub>2</sub>(111). *Phys. Chem. Chem. Phys.* 16, 24165–24168 (2014).
41. Nolan, M. & Watson, G. W. The surface dependence of CO adsorption on ceria. *J. Phys. Chem. B* 110, 16600–16606 (2006).
42. Yang, X. F. et al. Low pressure CO<sub>2</sub> hydrogenation to methanol over gold nanoparticles activated on a CeO<sub>x</sub>/TiO<sub>2</sub> interface. *J. Am. Chem. Soc.* 137, 10104–10107 (2015).
43. Li, H. Y., Wang, H. F., Guo, Y. L., Lu, G. Z. & Hu, P. Exchange between sub-surface and surface oxygen vacancies on CeO<sub>2</sub>(111): a new surface diffusion mechanism. *Chem. Commun.* 47, 6105–6107 (2011).
44. Chu, D. R., Wang, Z. Q. & Gong, X. Q. Theoretical insights into CO oxidation activities on CeO<sub>2</sub>(111) steps. *Surf. Sci.* 722, 122096 (2022).
45. Li, C. et al. Carbon monoxide and carbon dioxide adsorption on cerium oxide studied by Fourier-transform infrared spectroscopy. Part 1.—Formation of carbonate species on dehydroxylated CeO<sub>2</sub>, at room temperature. *J. Chem. Soc. Faraday Trans.* 85, 929–943 (1989).
46. Li, N. et al. Size effects of ZnO nanoparticles in bifunctional catalysts for selective syngas conversion. *ACS Catal.* 9, 960–966 (2019).
47. Sun, J. J. et al. Controllable assembly of CeO<sub>2</sub> micro/nanospheres with adjustable size and their application in Cr(VI) adsorption. *Mater. Res. Bull.* 75, 110–114 (2016).
48. Perdew, J. P., Burke, K. & Ernzerhof, M. Generalized gradient approximation made simple. *Phys. Rev. Lett.* 77, 3865–3868 (1996).
49. Perdew, J. P., Burke, K. & Ernzerhof, M. Generalized gradient approximation made simple. *Phys. Rev. Lett.* 78, 1396–1396 (1997).
50. Kresse, G. & Joubert, D. From ultrasoft pseudopotentials to the projector augmented-wave method. *Phys. Rev. B* 59, 1758–1775 (1999).
51. Dudarev, S. L., Botton, G. A., Savrasov, S. Y., Humphreys, C. J. & Sutton, A. P. Electron-energy-loss spectra and the structural stability of nickel oxide: An LSDA+U study. *Phys. Rev. B* 57, 1505–1509 (1998).
52. Da Silva, J. L. F., Ganduglia-Pirovano, M. V., Sauer, J., Bayer, V. & Kresse, G. Hybrid functionals applied to rare-earth oxides: The example of ceria. *Phys. Rev. B* 75, 045121 (2007).
53. Huang, M. & Fabris, S. CO adsorption and oxidation on ceria surfaces from DFT+U calculations. *J. Phys. Chem. C* 112, 8643–8648 (2008).
54. Loschen, C., Carrasco, J., Neyman, K. M. & Illas, F. First-principles LDA+U and GGA+U study of cerium oxides: Dependence on the effective U parameter. *Phys. Rev. B* 84, 199906 (2007).
- Program of China (2022YFA1503802, F.Y.) and Shanghai-XFEL Beamline Project (SBP) (31011505505885920161A2101001, Z.L.). The authors thank the support from the Analytical Instrumentation Center, at ShanghaiTech University and BL02B01 of the Shanghai Synchrotron Radiation Facility (SSRF) supported by the National Natural Science Foundation of China (11227902, Z.L.). DFT calculations were performed at Brookhaven National Laboratory, which was supported by the U.S. Department of Energy (DOE), Office of Science, Office of Basic Energy Sciences, Division of Chemical Sciences, Biosciences and Geosciences, under contract No. DE-SC0012704 (P.L.).

### Author contributions

W.S., Y.Z., and Z.W.Z. contributed equally to this work. Y. Z. carried out STM/XPS experiments. Z.W.Z. and P.L. carried out DFT calculations. W.S. carried out model catalytic tests and quasi-in-situ XPS experiments. W.S., N.L., and F.J. carried out the powder catalytic measurements. W.S. carried out FT-IR experiments. Y.S.L., Y.C., and Y.J.L. participated in SRPES experiments. Z.Y.Z. carried out NAPXPS experiments. Z.L., X.P., Q.F., and C.W. participated in the discussion and analysis of experimental results. W.S., Y.Z., Z.W.Z., P.L., and F.Y. analyzed the data and wrote the draft. F.Y. constructed and wrote the paper. X.B. and F.Y. designed and supervised the project.

### Competing interests

The authors declare no competing interests.

Correspondence and requests for materials should be addressed to Fan Yang.

Peer review information *Nature Communications* thanks Gyeong-Su Park and the other anonymous reviewers for their contribution to the peer review of this work. A peer review file is available.

Publisher's note Springer Nature remains neutral with regard to jurisdictional claims in published maps and institutional affiliations.

© The Author(s) 2024

### Acknowledgements

This work was financially supported by the National Natural Science Foundation of China (21991152 (Z.L.), M-0384 (F.Y.)), National Key R&D